

From $y=0$ to $y=3$: Recent Results from BRAHMS

I.G. Bearden^a for the BRAHMS Collaboration

^aNiels Bohr Institute, University of Copenhagen, Copenhagen, Denmark

Results from the BRAHMS collaboration for the 200 GeV Au+Au RHIC run 2 in 2001 are presented. We discuss the pseudo-rapidity distribution of charged particles. The emphasis, however, is on new results of rapidity densities for identified π^\pm , K^\pm and p, \bar{p} as a function of particle rapidity. In addition, we present antiparticle to particle ratios.

1. The Experimental Setup

BRAHMS consists of two small acceptance magnetic spectrometers, as depicted in Fig. 1, one of which operates near mid-rapidity (MRS) (95° – 30° with respect to the beam direction) and one (FS) at smaller angles (2.3° – 30°) for measuring particles produced at forward rapidities. Together, these spectrometers cover a rapidity range of $-0.1 < y < 4$ for pions and $-0.1 < y < 3.4$ for protons. Details of the experiment can be found elsewhere [1].

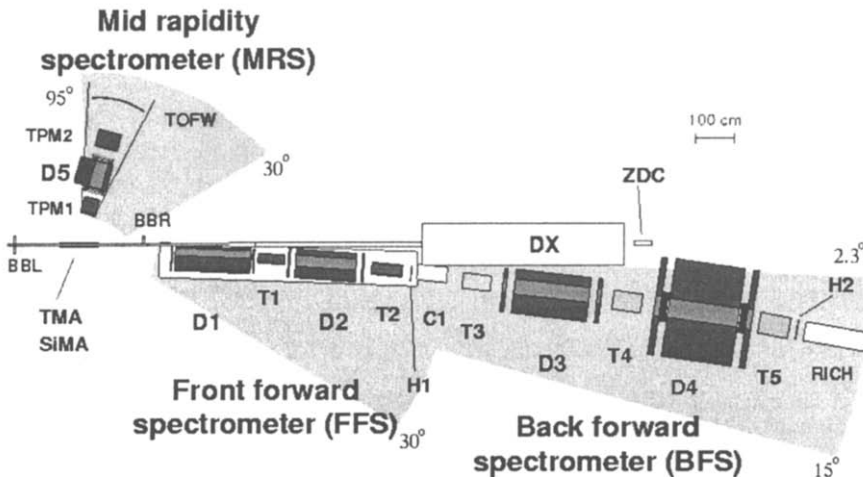


Figure 1. Layout of the BRAHMS experiment. The shaded regions indicate the angular coverage of the various spectrometer segments. Tracking detectors are labeled TPM1, TPM2, T1–T5, and dipole magnets D1–D5.

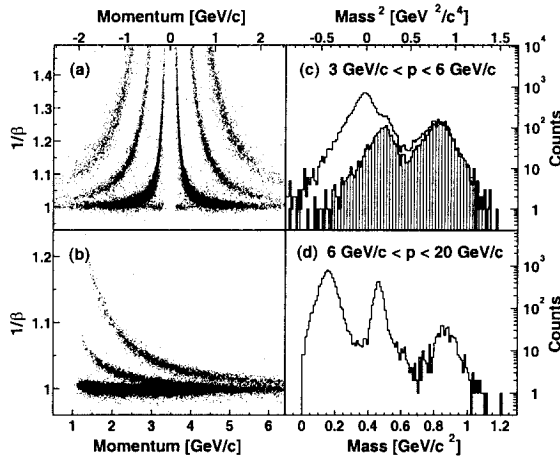


Figure 2. Particle identification capability of BRAHMS. (a) and (b) Separation between pions, kaons, and protons. The MRS (a) is at 90 deg. and both charges are accepted. The FS (b) is here positioned at 12 degrees. (c) Mass-squared spectrum in the FS from time-of-flight measurements using H1. In the shaded histogram, pions have been vetoed by C1. (d) Mass spectrum obtained with the RICH.

The Mid-Rapidity Spectrometer (MRS) consists of two time projection chambers (TPM1, TPM2) and a dipole magnet (D5), for determining particle momenta. This assembly is followed by a segmented scintillator time-of-flight wall (TOFW), with a time resolution $\sigma_{tof} \approx 75$ ps, 4.5 m from the nominal interaction point (IP) for measuring particle velocity. Requiring a $\pm 2\sigma_{tof}$ cut around the expected flight time, π - K separation is achieved up to a momentum of 2.3 GeV/c and K - p separation up to 3.9 GeV/c. The Front Forward Spectrometer (FFS) consists, in order, of a dipole magnet (D1), a TPC (T1), a second dipole magnet (D2), a second TPC (T2), a time-of-flight wall (H1) and a threshold gas-Cherenkov detector (C1). At small polar angles (from 2.3° to 15°), where the mean momentum of particles is large, an additional section (BFS) is employed. This comprises two dipole magnets (D3, D4), three drift chambers (T3, T4, T5), a time of flight wall (TOF2) and a ring imaging Cherenkov detector (RICH). TOF1 (situated 8.6 m from the IP) and TOF2 (at 18 m from the IP) allow for K - p separation up to $p=5.5$ and 8 GeV/c, respectively. C1 identifies pions in the range from $p = 3$ to 9 GeV/c and the RICH allows for π - K separation up to $p = 25$ GeV/c and K - p separation from $p=10$ to $p=35$ GeV/c. The performance of the PID in BRAHMS is summarized in fig. 2. A plot of the BRAHMS acceptance in (y, p_t) for the data presented here can be found in ref [2].

In addition to the two spectrometers, there are several detectors for characterizing the global properties of the reaction. The Beam-Beam counters (BBC, BBL and BBR in Fig. 1) measure charged hadrons in the pseudo-rapidity range $2.1 < |\eta| < 4.7$. The good timing resolution of the BBCs allows for the accurate determination of the collision position ($\sigma_{VTX} \approx 0.65$ cm) and the start for the spectrometer TOF walls ($\sigma_t \approx 35$ ps).

The Zero Degree Calorimeters (ZDC) at $\pm 18\text{m}$, measure spectator neutrons from the collisions. One can determine the location of the collision to a precision of $\approx 2.5\text{ cm}$ via the time difference of the ZDC signals. There are two multiplicity arrays, one consisting of Si strip detectors (SiMA) covers $-2.2 < \eta < 2.2$ and one of plastic scintillator tiles (TMA) covering the range $-2.0 < \eta < 2.0$. It is possible to extend the coverage of these devices to $-3.0 < \eta < 3.0$ by exploiting the spread in the collision vertex location. The utility of this is that it enables the multiplicities given by the SiMA, TMA, and BBC to be compared in the same pseudo-rapidity range. The three systems give consistent results.

2. Charged particle pseudo-rapidity densities

In high energy nuclear collisions, particles can be produced by both hadronic (“soft”) and partonic (“hard”) processes. One experimental tool to try to address the extent to which these different processes contribute is to systematically measure particle production as a function of centrality over a broad range in pseudo-rapidity, $\eta = -\ln \tan \theta/2$. In Fig. 3 we present $dN_{ch}/d\eta$ as a function of pseudo-rapidity for a variety of centrality classes [3]. For comparisons to other systems, in particular to $p + \bar{p}$ collisions, one can scale the multiplicity by number of participant pairs (N_{part}). Figure 4 shows that this scaled multiplicity is independent of both centrality and beam energy in the η range from 0.5 to 1.5 units less than the beam rapidity. $dN_{ch}/d\eta/(N_{part}/2)$ increases from 130 GeV to 200 GeV, indicating that the kinetic energy goes to increased particle production near mid-rapidity.

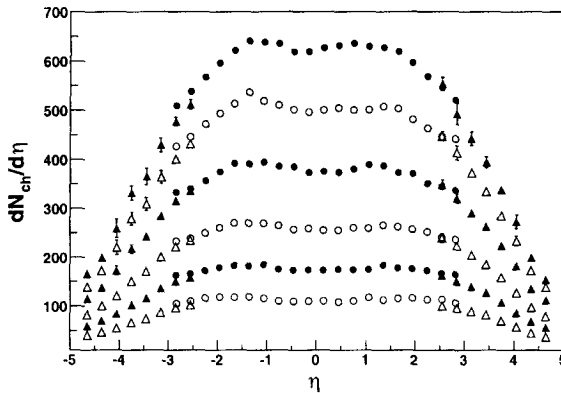


Figure 3. $dN_{ch}/d\eta$ for centrality ranges 0-5% (top), 5-10%, 10-20%, 20-30%, 30-40%, and 40-50% (bottom). The statistical errors are shown where larger than the data points. Systematic errors are 8% for SiMA (circles), and 20% for BBC results (triangles).

Figure 5 shows a comparison between the BRAHMS data (open circles) and model calculations, appropriately scaled data from 200 GeV $p + \bar{p}$ collisions are also shown. The solid line from Kharzeev and Levin [4], is a QCD calculation in which particle production saturates due to a saturation in the number of gluon collisions. AMPT [5], shown by the dashed lines is a cascade model based on HIJING, but including re-scattering of the

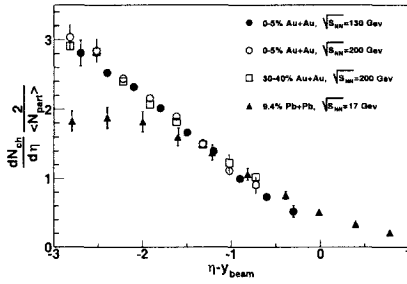


Figure 4. $dN_{ch}/d\eta$ normalized to the number of participant pairs for the 0-5% central (open circles) and 40-50% central (open squares). Solid circles correspond to data from 0-5% central Au+Au collisions at $\sqrt{s_{NN}} = 130$ GeV [6], solid triangles to data from 0-9.4% central Pb+Pb collisions at $\sqrt{s_{NN}} = 17$ GeV [7].

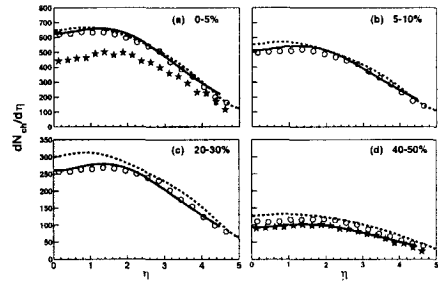


Figure 5. $dN_{ch}/d\eta$ for centrality ranges 0-5% (a), 5-10% (b), 20-30% (c), and 40-50% (d). Predictions from AMPT (dashed) and Kharzeev and Levin (solid) are shown for comparison. Suitably scaled results from $p\bar{p}$ collisions are shown in (a) and (d) as stars.

produced particles. Within the errors on our data and the models shown, it is not possible to favor one model over the other.

3. Identified particle spectroscopy

The primary strength of BRAHMS is the study of identified particles (π, K, p) over a broad range of rapidities and a large transverse momentum range. In this proceeding, we present preliminary results on particle yields at both mid-rapidity and forward ($y_\pi \approx 3$) rapidities. The details of these can be found in other contributions to these proceedings [2, 8], with only the highlights presented here. In addition, we discuss more mature results on antiparticle to particle ratios which are described in more detail in ref [9].

3.1. Antiparticle to Particle Ratios

We measure $\langle d^2n/dp_T dy \rangle \Delta p_T \Delta y$, where the averaging is over phase space, $\Delta p_T \Delta y$. The ratios are of the normalized numbers of detected particles. Our results for the 20% most central collisions are summarized in the top panel of Fig. 6. At mid-rapidity, the ratios range from 0.75 ± 0.04 (\bar{p}/p), 0.95 ± 0.05 (K^-/K^+) to 1.01 ± 0.04 (π^-/π^+). Toward forward rapidities, the pion ratio remains constant, while both the K and p ratios decrease with increasing rapidity, to $K^-/K^+ = 0.67 \pm 0.06$ and $\bar{p}/p = 0.23 \pm 0.03$ at $y \approx 3$. This behavior is expected from a collision zone which is (very nearly) net-baryon free at midrapidity and particle production is due predominantly from pair production. Moving away from this central zone, the ratios become ever more influenced by the baryon content of the original nuclei. Recent PHOBOS measurements [10] at mid-rapidity are consistent with the measurements presented here.

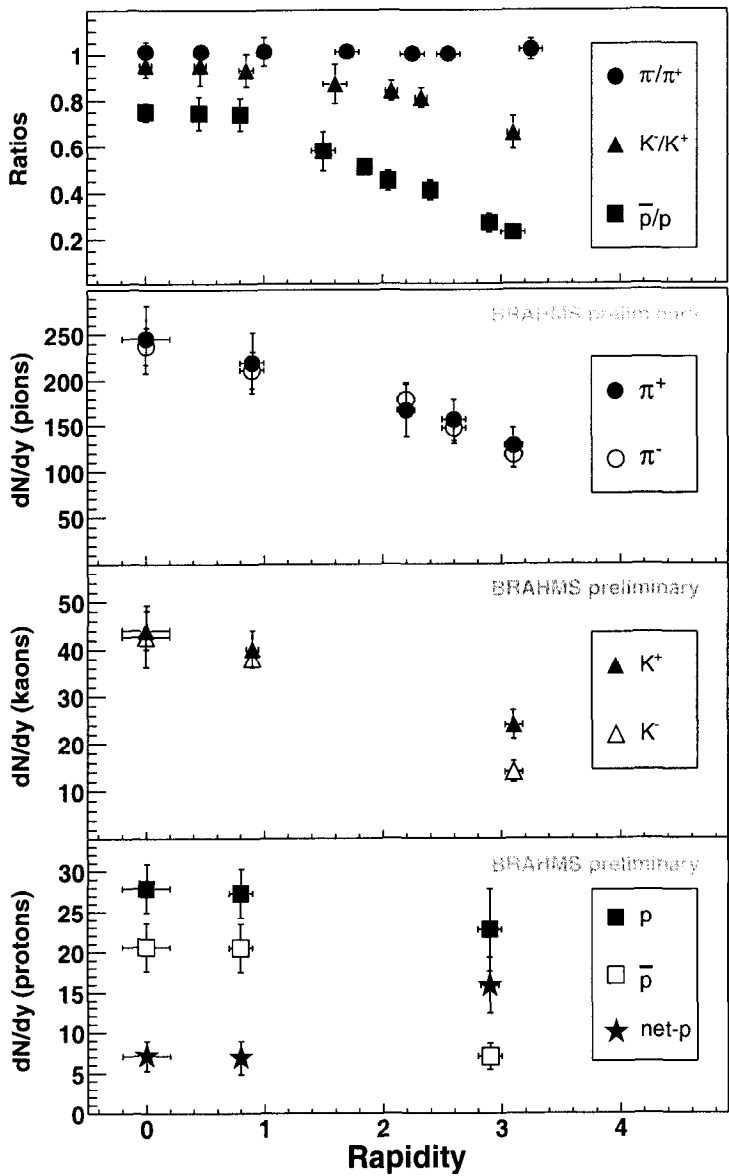


Figure 6. Top: Antiparticle-to-particle ratios as a function of rapidity (20% centrality). The three lower panels show the rapidity dependence of the yields (dN/dy) for pions, Kaons and protons, respectively (10% centrality). The errors are combined statistical and systematic. The horizontal bar indicates the rapidity range covered.

3.2. Spectra and Yields

BRAHMS has also measured transverse momentum spectra for π^\pm , K^\pm , p and \bar{p} . Examples of the measured spectra can be found in [2,8]. In the lower panels of Fig. 6 we present the rapidity density, dN/dy , for π^\pm , K^\pm and p, \bar{p} . All data shown are from the 10% most central collisions as measured by the TMA. The mesons exhibit broad distributions and the antiproton perhaps a narrower distribution peaked at midrapidity, while the rapidity density we measure for protons decreases only slightly from $y = 0$ to $y \approx 3$. The full rapidity dependence has not yet been fully characterized, however we are currently analyzing data from RHIC Run II which will fill in the rapidity regions between $y = 0$ and $y \approx 1$, and between $y \approx 1$ and $y = 3$. We note that the present limited data for pions and kaons can be described with gaussian rapidity density distributions, such a distribution is worse for antiprotons, which appear to be flat over at least $|y| < 1$.

4. Discussion

The measured set of particle ratios at midrapidity can be discussed in terms of a model based on the assumption of a system in chemical and thermal equilibrium as has been done at AGS [15] and SPS [16] energies. Recently, particle ratios measured at $\sqrt{s_{NN}} = 130$ GeV in the midrapidity region have been analyzed in a statistical model requiring baryon number, strangeness and charge conservation [17]. The free parameters of the model are the temperature T at which chemical freeze out occurs and the baryon (or light quark)

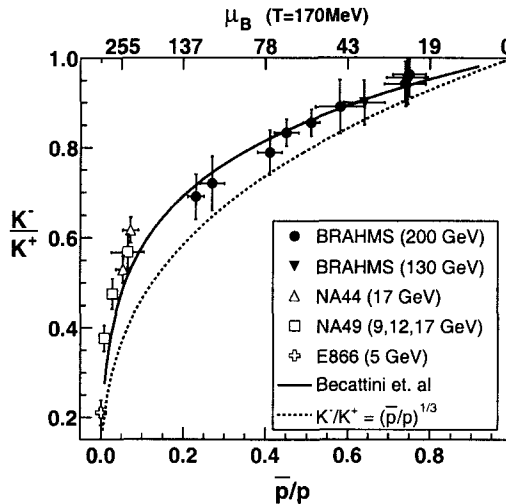


Figure 7. Correlation between kaon and proton antiparticle-to-particle ratios. The NA44 and NA49 data are from Refs. [11] and [12], respectively. The E866 data are from Ref. [13]. The dashed line shows the relation $K^-/K^+ = (\bar{p}/p)^{1/4}$ (obtained by fitting the data) and the dotted line shows $K^-/K^+ = (\bar{p}/p)^{1/3}$. The full line shows the thermal prediction of Becattini et al.[14].

chemical potential $\mu_B = 3\mu_q$. Values of $T = 174 \pm 7$ MeV and $\mu_B = 46 \pm 5$ MeV were found. In Ref. [17] a parametrization as a function of energy is proposed leading to a prediction for $\sqrt{s_{NN}} = 200$ GeV of $T = 177 \pm 7$ MeV, $\mu_B = 29 \pm 8$ MeV and thus $\bar{p}/p = 0.752$, $K^-/K^+ = 0.932$, and $\pi^-/\pi^+ = 1.004$. The excellent numerical agreement between these calculations and the present measurements is rather striking. Within this approach, the near constancy of the temperature for chemical freeze-out found at SPS, at lower RHIC energies, and at the present energy can be associated with a fixed deconfinement transition temperature and the establishment of chemical equilibrium during hadronization. The small value of the chemical potential indicates a small net baryon density at midrapidity, in agreement with the BRAHMS measurement.

A comparison of the K^-/K^+ and \bar{p}/p ratios over a large range in rapidity and collision energy shows a remarkable correlation as shown in Fig. 7. The K^-/K^+ and \bar{p}/p ratios are measured at slightly different rapidities, so the K^-/K^+ ratios in Fig. 7 are interpolated to the y value of the \bar{p}/p measurements. Also shown are similar ratios determined at AGS [13] and SPS energies [12,11]. The figure displays a fairly smooth relationship between the ratios from AGS and SPS to RHIC. Good agreement is found by comparing the present data with the thermal model of Becattini et al. [14], which is based on SPS results integrated over the full phase space, and assumes a chemical freezeout temperature of $T = 170$ MeV. Within the framework of the statistical model, and assuming that the particle sources corresponding to the different rapidity regions sampled in our experiment are characterized by this temperature, fig. 7 indicates that the baryon chemical potential decreases from $\mu_B \approx 130$ MeV, at $y \approx 3$, to $\mu_B \approx 25$ MeV, at $y=0$.

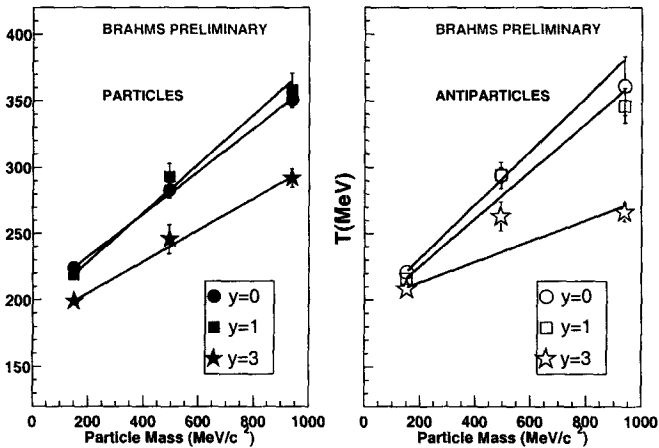


Figure 8. Inverse slope parameters, T , vs particle mass for $y = 0$, $y = 1$ and $y = 3$. The lines are the results of fits using a linear fit in mass, as described in the text.

From the measured spectra, which are presented in [2,8], we can determine the inverse slope parameters, T , from exponential fits to the transverse mass spectra. It is interesting to investigate the behavior of this “temperature” parameter as a function of particle mass over the range of measured rapidities we measure. The slope of the particle mass vs. T line gives an indication of the amount of radial flow in the particle source. Figure 8 shows the results for $y = 0$, $y \approx 1$, and $y \approx 3$. The rapidities are the same for π, K, p at $y = 0$ and while this is of course not the case in the other settings, for the purposes of this plot we ignore the small ($\delta y = 0.2$) difference in π and proton rapidity at $y \approx 3$. The result is quite striking: There is no discernible difference in the $y = 0$ and $y \approx 1$ data, but a large drop in the slope from mid to forward rapidity. Fitting the three sets of data to the equation $T_{eff} = T + m\beta^2$, we find that at $y = 0$, $T = 200 \pm 5$ MeV and $\beta = 0.40 \pm 0.01$, and $y = 1$, $T = 190 \pm 5$ MeV and $\beta = 0.43 \pm 0.02$, while for $y \approx 3$ $T = 181 \pm 4$ MeV and $\beta = 0.34 \pm 0.01$. The anti-particles exhibits a similar trend. The term T , which can be associated with the kinetic freezeout temperature [19], remains nearly constant, while the extracted β , which is the radial expansion velocity, drops by 15%. This indicates that the radial flow is decreased significantly from mid to forward rapidities.

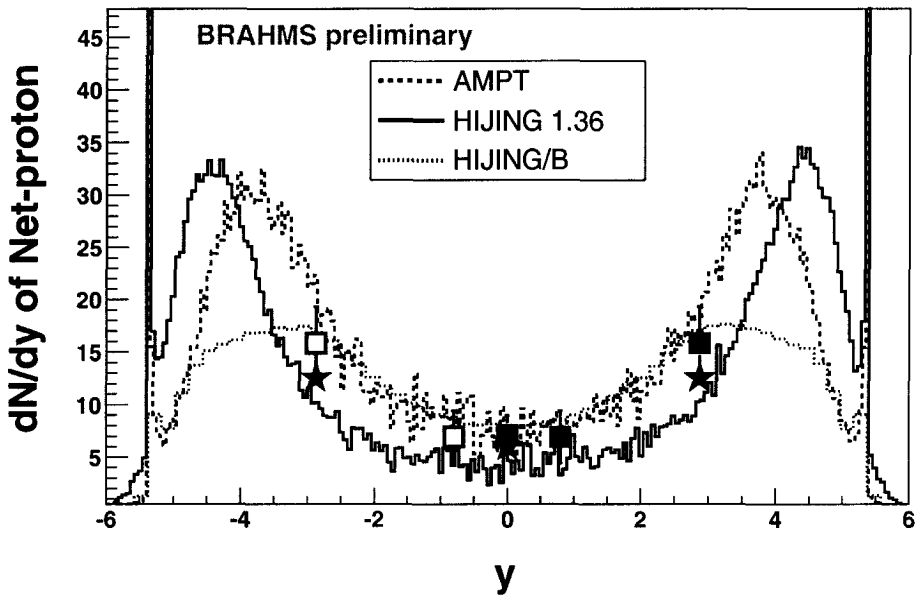


Figure 9. Net-proton rapidity density versus rapidity compared to models. The open symbols are reflections of the measurements. The stars (at $y = 0$ and $y \approx 3$) indicate the net-protons corrected for Λ feed-down (as described in [8]). The dashed line is AMPT, the solid line is HIJING [20], and the dotted line HIJING/B.

Finally, we compare the measured net-proton density to model calculations in Fig. 9. As can be seen in the figure, both AMPT and HIJING/B reproduce our data slightly better than HIJING. This implies that HIJING underestimates, though perhaps only slightly, the amount of stopping in these collisions, since both AMPT and HIJING/B are based on HIJING but include mechanisms (rescattering and baryon junctions, respectively) which increase stopping. It is also interesting that models which include a large amount of rescattering (RQMD, UrQMD [21]) predict a much too large net proton density near mid-rapidity at RHIC energies while reproducing the results from SPS energies extremely well.

Acknowledgements

This work was supported by the Division of Nuclear Physics of the Office of Science of the U.S. Department of Energy, the Danish Natural Science Research Council, the Research Council of Norway, the Jagiellonian University Grants, and the Romanian Ministry of Research.

REFERENCES

1. M. Adamczyk *et al.*, BRAHMS Collaboration, Nuclear Instruments and Methods, to be published.
2. D. Ouerdane, BRAHMS Collaboration, these proceedings.
3. I. G. Bearden *et al.*, BRAHMS Collaboration, Phys. Rev. Lett. **88**, 202301 (2002).
4. D. Kharzeev and E. Levin, Phys. Lett. B **523**, 79 (2001)
5. B. Zhang *et al.*, Phys. Rev. **C61**, 067901 (2000).
6. I. G. Bearden *et al.*, BRAHMS Collaboration, Phys. Lett. **B523**, 227 (2001).
7. P. Deines-Jones *et al.*, Phys. Rev. C **62**, 014903 (2000).
8. J. H. Lee, BRAHMS Collaboration, these proceedings.
9. I. G. Bearden *et al.*, BRAHMS Collaboration, Submitted to Phys. Rev. Lett., nucl-ex/0207006.
10. B. B. Back *et al.*, PHOBOS Collaboration, Submitted to Phys. Rev. C (2002), nucl-ex/0206012.
11. I. G. Bearden *et al.*, NA44 Collaboration, Phys. Rev. C **66**, 044907 (2002).
12. Y. Afanasiev *et al.*, NA49 Collaboration, nucl-ex/02050002; J. Bächler *et al.*, Nucl. Phys. **A661**, 45 (1999).
13. L. Ahle *et al.*, E866 Collaboration. Phys. Rev. Lett. **81**, 2650 (1998) and Phys. Rev. **C60**, 044904 (1999).
14. F. Becattini *et al.*, Phys. Rev. **C64**, 024901 (2001) and private communication.
15. P. Braun-Munzinger, J. Stachel, J. P. Wessels, N. Xu, Phys. Lett. **B344**, 43 (1995).
16. P. Braun-Munzinger, J. Stachel, J. P. Wessels, N. Xu, Phys. Lett. **B365**, 1 (1996)
17. P. Braun-Munzinger *et al.*, Phys. Lett. **B518**, 41 (2000).
18. C. Adler *et al.*, STAR Collaboration, Phys. Rev. Lett **87**, 262302 (2002).
19. I. G. Bearden *et al.*, NA44 Collaboration, Phys. Rev. Lett. **78**, 2080 (1997).
20. S. E. Vance, M. Gyulassy and X. N. Wang Nucl. Phys. **A638**, 395 (1998).
21. M. J. Bleicher *et al.*, Phys. Rev. **C62**, 24904 (2000).